Iranian Journal of Fuzzy Systems

Volume 23, Number 1, (2026), pp. 125-145

Original paper

University of Sistan and Baluchestan

Safe fuzzy longitudinal and lateral controller design for high-speed lane-change maneuvers in autonomous vehicles using the Pacejka tire model

M. Nouri Manzar [1], M. R. Kamali Ardakani [2] and M. Pourgholi [3]

[1,3] *Faculty of Electrical Engineering, Shahid Beheshti University, Tehran, Iran.*
[2] *Faculty of Automation Engineering, University of Bologna, Bologna, Italy.*

m_pourgholi@sbu.ac.ir, mohammadreza.kamali@studio.unibo.it, m_pourgholi@sbu.ac.ir

Abstract

High-speed lane-change maneuvers in autonomous vehicles require control strategies that remain safe and well-damped under strongly nonlinear tire–vehicle dynamics and uncertain interactions with surrounding traffic. This paper proposes a stability-aware fuzzy control framework built on a nonlinear single-track (bicycle) vehicle model augmented with an enhanced semi-empirical Pacejka tire formulation to capture the coupled longitudinal–lateral–yaw behavior under realistic tire-condition effects. Two coordinated Mamdani type-1 fuzzy controllers are designed: one generates the steering command for lateral–yaw regulation and trajectory tracking, and the other produces the longitudinal acceleration command for speed adaptation and headway preservation. All membership-function parameters and rule weights are jointly tuned via constrained simulation-based optimization using the Slime Mould Algorithm (SMA), while actuator bounds and an explicit hard collision-avoidance constraint are enforced throughout the maneuver horizon. A Lyapunov-inspired penalty is embedded in the objective to suppress oscillations and promote well-damped responses. Simulations of high-speed lane changes (up to 72 km/h) show rapid convergence of lateral and longitudinal errors (∼2–3 s over a ∼450 m path), smooth control actions, and collision-free behavior. Compared with an unoptimized fuzzy baseline, the tuned design reduces peak lateral deviation by ∼35% and yaw-rate oscillations by ∼40%. Monte-Carlo trials with parametric uncertainty, measurement noise, and actuator delays further confirm repeatable closed-loop performance and robust safety margins in mixed-traffic scenarios.

Keywords: Autonomous vehicles, lane change, fuzzy logic control, metaheuristic optimization, Pacejka tire model, robustness, safety constraints.

1 Introduction

The rapid proliferation of electronic devices and sensors in the automotive industry has accelerated advances in autonomous vehicles (AVs). Self-driving cars promise to optimize traffic flow, reduce congestion, and provide safer mobility-especially for drivers who are fatigued or otherwise impaired. Despite this progress, fully reliable and safe AV operation remains elusive. Over the past few decades, production vehicles have adopted advanced driver assistance systems (ADAS), adaptive cruise control (ACC), and dynamic stability control (DSC), enabling various forms of semi-autonomous functionality [12]. Yet safe high-speed lane changing remains a central challenge: the vehicle must track a desired trajectory precisely, reason under uncertainty, and interact safely with human-driven vehicles in dynamic, often congested environments. Notably, human error still contributes to roughly 90% of expressway accidents, underscoring the societal importance of robust AV lane-change control [2].

Corresponding Author: M. Pourgholi
Received: July 2025; Revised: December 2025; Accepted: January 2026.
https://doi.org/ 10.22111/ijfs.2026.52694.9307

AV motion and behavior planning has seen diverse algorithmic paradigms. Software architectures leveraging Voronoi diagrams and state-lattice methods enable efficient path planning and obstacle avoidance during lane changes [16]. Broader surveys organize AV–HV (human-vehicle) interaction models at microscopic, mesoscopic, and macroscopic levels and discuss conflict-resolution strategies such as first-come-first-served (FCFS) and Monte Carlo Tree Search (MCTS) at merges [21]. Multi-objective formulations, cubic-polynomial trajectories evaluated with TOPSIS-balance safety, comfort, and efficiency for overtaking at 50–80 km/h [23], while high-speed lane-change studies (up to 140 km/h) couple dynamic vehicle and tire models with robust controllers to preserve stability [8]. Probabilistic decision frameworks encode perception and intent uncertainty over long freeway drives [1]; models such as SITRAS combine forced and cooperative lane changes under congestion, improving flow–speed relations via gap acceptance and courtesy behaviors [5]. Low-complexity pipelines assess maneuver desirability via utility functions, select reachable gaps, and plan trajectories with MPC-based quadratic programs-validated on a Volvo V60 [11]. On the execution side, cooperative (CLCE) and forced (FLCE) longitudinal models derived from Gipps' crash-avoidance theory, calibrated on NGSIM, use dynamic lane-weighting to outperform prior baselines [20].

In connected and automated driving, recent studies have also emphasized co-designing trajectory planning and tracking to balance multiple objectives such as energy consumption, passenger comfort, and tracking accuracy. Precup et al. [13] proposed a two-stage optimization framework for a connected autonomous electric bus (CAEB) in signalized intersection scenarios with human-driven vehicles, where a discrete-time segment-based trajectory planning stage is combined with a continuous-time cruise-control stage to optimize energy, comfort, and tracking performance.

A recent comprehensive survey by Kamil et al. [6] reviewed the evolution of fuzzy logic-based control systems for intelligent vehicles, emphasizing their ability to manage uncertainty, nonlinearity, and human-like reasoning in autonomous navigation. The authors highlighted fuzzy control's successful use in unmanned ground, underwater, and aerial vehicles, as well as its growing importance in intelligent transportation systems (ITS). This overview reinforces that fuzzy logic remains a core technology for interpretable and adaptive AV decision and control architecture. Complementary studies have demonstrated how fuzzy reasoning can be enhanced through optimization or hybrid frameworks. Rodríguez-Abreo et al. [14] optimized fuzzy controller gains for an unmanned aerial vehicle (UAV) using a Genetic Algorithm, achieving significant reductions in trajectory-tracking error compared with manually tuned controllers. These studies collectively underscore the effectiveness of combining fuzzy reasoning with optimization approach central to the present work. Further research in intelligent control highlights the synergy between optimized fuzzy systems and stable nonlinear control. Hentout et al. [4] presented a complete navigation and control system for mobile robots in indoor static and dynamic environments, where a Deterministic Constructive Algorithm (DCA) computed the shortest path and an Efficient Fuzzy Logic Controller (EFLC) guided the robot safely around unforeseen obstacles. Their simulations demonstrated that this hybrid structure effectively balanced global path optimization with real-time adaptability, confirming the capability of fuzzy controllers to mimic human reasoning for stable navigation under uncertainty. Similarly, Wen and Wang [18] investigated the stabilization of nonlinear electromagnetic suspension systems in maglev trains using an improved cascade control strategy that combined Lyapunov, sliding-mode, and PID controllers. Their results showed that such a structured combination of simple control laws could achieve both robustness and stability without resorting to overly complex algorithms principle that closely parallels the requirements of AV lane-change control, where lightweight yet reliable architectures are essential.

Building on this foundation, the present work introduces a robust control framework for autonomous vehicles capable of performing collision-free high-speed lane-change maneuvers while dynamically adapting the longitudinal speed to surrounding traffic conditions. The framework integrates two fuzzy-logic-based controllers governing longitudinal acceleration and the other lateral steering-formulated around an enhanced Pacejka tire model that captures the nonlinear coupling among longitudinal, lateral, and yaw dynamics. The membership functions and rule weights of both controllers are optimized through a multi-objective cost function minimized via the Slime Mould Algorithm (SMA). In addition, safety-oriented rule sets are embedded to prevent potential collisions during lane-change transitions, thereby ensuring stable and reliable autonomous-vehicle operation under varying driving scenarios. Although high-speed lane-change control has been extensively studied using planning-oriented optimization and robust control methods, most existing works treat vehicle dynamics in a simplified or decoupled manner. Few studies simultaneously integrate a physics-based tire model that captures nonlinear longitudinal-lateral-yaw coupling with a co-designed fuzzy controller optimized in a unified framework. Conventional fuzzy or optimal control schemes often rely on linearized tire dynamics or tune controller parameters separately, which limit their accuracy and stability at high speeds. This research addresses the gap by combining an enhanced Pacejka tire model with an SMA-optimized dual fuzzy-controller architecture that incorporates stability-aware cost shaping to ensure precise and robust maneuvering under dynamic driving conditions.

To highlight the novelty of the proposed approach, Table 1 presents a taxonomy and comparison of representative fuzzy-based control methods developed for autonomous-vehicle lane-change and navigation tasks.

Table 1: Taxonomy and comparison of representative fuzzy-based control methods for autonomous-vehicle lane-change and navigation.

Ref / Year	Method Type	Model / Tire	Optimization / Safety	Key results / remarks
[16] Naranjo et al., 2008	Type-1 fuzzy control	Dynamic vehicle model; no tire model (simplified)	Manual rule tuning; no explicit stability proof	Smooth maneuvering; validated in real vehicle; baseline fuzzy lane-change controller
[17] Hongtao Xue et al., 2019	Picture fuzzy system	In-wheel motor system (EV); no tire model	Multi-criteria decision fusion; safety indices (operation reliability)	Focuses on EV component safety, not control synthesis or dynamics
[18] Haider et al., 2022	ANFIS navigation	Mobile robot (indoor); no tire model	Hybrid learning (GD + LS); collision avoidance only	Demonstrates fuzzy learning concept; not applicable to high-speed vehicle dynamics
Present work (2025)	Dual fuzzy logic + metaheuristic optimization	Nonlinear single-track vehicle model; enhanced Pacejka semi-empirical tire model	Slime Mould Algorithm (SMA); Lyapunov-inspired stability penalty; hard collision-avoidance constraint	≈35% reduction in lateral deviation; ≈40% reduction in yaw oscillation

2 Vehicle dynamic

In the following, a nonlinear dynamic model that captures the coupling among longitudinal, lateral, and yaw motions and ensures reliable performance across a broad spectrum of vehicle operating conditions is presented.

2.1 Longitudinal dynamics

Accurate regulation of the vehicle's longitudinal velocity is critical for maintaining safe headways during lane-change maneuvers. The vehicle's model diagram is depicted in Fig. 1. This requirement is captured by the longitudinal dynamic model, presented in Eq. (1), which explicitly incorporates aerodynamic drag effects at high speeds to enhance the fidelity of the drag coefficient's dynamic response [8].

$$m\dot{v}_x = F_{x,f}\cos\delta - F_{y,f}\sin\delta + F_{x,r} - F_{\text{drag}}. \tag{1}$$

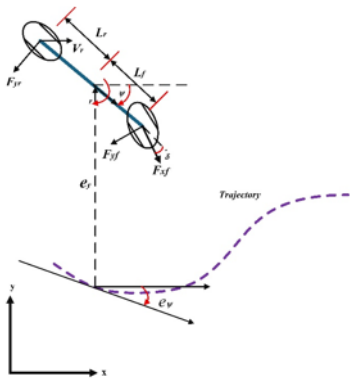

Figure 1: A diagram of vehicle model.

where m is the vehicle's mass, $\dot{v}_x$ is longitudinal acceleration, $F_{x,f}$ and $F_{y,f}$ are the front tire's longitudinal and lateral forces, δ is the steering angle, and the last term accounts for aerodynamic drag with air density ρ, drag coefficient C_d, frontal area A, and velocity v_x. The drag force is given by Eq. (2).

$$F_{\text{drag}} = \frac{1}{2}\rho C_d A v_x^2. \tag{2}$$

The longitudinal force at the front tire ($F_{x,f}$) is derived from the commanded acceleration (a_x), adjusted for the tire's peak grip under varying conditions, as shown in Eq. (3) [8]:

$$F_{x,f} = ma_x \frac{\mu_{\max,f}}{\mu_{\max,f_0}}. \tag{3}$$

where $\mu_{\max,f}$ is the adapted peak grip coefficient for the front tire, and $\mu_{\max,f_0}$ is the nominal peak grip. The rear longitudinal force ($F_{x,r}$) is zero, reflecting the front-wheel-drive configuration.

As mentioned, one of the critical aspects of an autonomous vehicle's lane-changing system is its ability to accurately manage the vehicle's speed. The system uses a commanded longitudinal acceleration, denoted as a_x, to specify how quickly the vehicle should speed up or slow down, akin to a driver adjusting the accelerator. This command is translated into the front tire's longitudinal force, adjusted for the tire's grip under varying conditions such as pressure or temperature. However, the actual change in the vehicle's speed, represented by the longitudinal acceleration $\dot{v}_x$, depends not only on this command but also on real-world factors like air resistance and the effects of steering. For instance, when the vehicle turns, some tire force is redirected sideways, slightly reducing the actual acceleration compared to the command value as captured by the drag and steering terms in the equation. By accurately modeling both the intended acceleration a_x and the resulting motion $\dot{v}_x$, our system ensures smooth, safe lane changes and maintains control at high speeds or worn tires.

2.2 Lateral and yaw dynamics

For lane changes in autonomous vehicles, precise control of lateral and yaw movements is essential to ensure safe and effective navigation. The Eq. (4) governs the lateral acceleration, where v_y is the lateral velocity, r is the yaw rate, $F_{y,r}$ is the rear lateral tire force, and $F_{y,f}$ is the front lateral force, driving the vehicle's sideways movement guided by steering and tire forces [8]:

$$m\left(\dot{v}_y + v_x r\right) = F_{y,f}\cos\delta + F_{y,r} + F_{x,f}\sin\delta. \tag{4}$$

The yaw dynamics, which dictate the vehicle's rotational motion about its vertical axis, are described by [14]:

$$I_z \dot{r} = l_f\left(F_{y,f}\cos\delta + F_{x,f}\sin\delta\right) - l_r F_{y,r}. \tag{5}$$

where I_z is the yaw moment of inertia (kg·m^2), l_f is the distance from the center of gravity (CoG) to the front axle (m), and l_r is the distance to the rear axle (m). The front tire forces contribute positively to yaw acceleration, promoting rotation, while the rear lateral force provides a stabilizing negative moment. The yaw angle error (e_ψ) and lateral position error (e_y) relative to a reference path is updated as follows [9]:

$$\dot{e}_\psi = r, \qquad \dot{e}_y = v_y + v_x e_\psi. \tag{6}$$

These equations track the vehicle's orientation and lateral deviation, enabling the control system to adjust steering to align with the target lane.

2.3 Normal load distribution

The normal loads on the front ($F_{z,f}$) and rear ($F_{z,r}$) tires are influenced by longitudinal acceleration due to weight transfer, as given by [8]:

$$\begin{aligned} F_{z,f} &= \frac{mg\,l_r}{l_f + l_r} - \frac{ma_x h}{l_f + l_r}, \\ F_{z,r} &= \frac{mg\,l_f}{l_f + l_r} + \frac{ma_x h}{l_f + l_r}, \end{aligned} \tag{7}$$

where g is the gravitational acceleration (m/s^2), and h is the height of the center of gravity (m). These equations ensure accurate force calculations, reflecting the shift in vertical load during acceleration or deceleration.

2.4 Pacejka tire model

In autonomous vehicles, tire-road interaction is of particular importance in lane changes. The enhanced Pacejka formulation [17] adopted here is a semi-empirical representation that combines experimental curve-fitting with analytical structure to describe the nonlinear coupling among longitudinal, lateral, and yaw dynamics. Unlike purely physical models, which require high-order thermomechanical parameters and are computationally intensive, the semi-empirical

Pacejka form captures key tire–road interactions through compact coefficients that can be adapted in real time. This semi-empirical model, integrated with single-track vehicle dynamics, considers tire pressure, tread depth, and temperature, and enhances stability and control. These equations are written for both the front and rear wheels. The subscript i indicates a general case: setting $i = f$ yields the equations for the front wheels and setting $i = r$ yields the equations for the rear wheels. Note that a_{ijk} and b_{ij} are the coefficients used in the Pacejka tire model.

Slip Angle Calculation Equation (8) shows the slip angle for the tire:

$$\begin{aligned} \alpha_f &= \delta - \arctan\left(\frac{v_y + l_f r}{v_x}\right), \\ \alpha_r &= -\arctan\left(\frac{v_y - l_r r}{v_x}\right). \end{aligned} \tag{8}$$

Peak Grip Coefficient Equation (9) is used to calculate the peak grip coefficient:

$$\mu_{y,\max,i} = \left[\left(a_{11}y_i^2 + a_{12}y_i + a_{13}\right)F_{z,i} + \left(a_{21}y_i + a_{22}\right)\right]\left(b_{11}z_i^2 + b_{12}z_i + b_{13}\right). \tag{9}$$

The cornering stiffness, a measure of the tire's lateral force response to slip angle, is computed using three terms. The first term ($\mathrm{Term}_{i,1}$) is a quadratic function of tire pressure (x_i) and tread depth:

$$\mathrm{Term}_{i,1} = \left(a_{311}y_i^2 + a_{312}y_i + a_{313}\right)x_i^2 + \left(a_{321}y_i^2 + a_{322}y_i + a_{323}\right)x_i + \left(a_{331}y_i^2 + a_{332}y_i + a_{333}\right). \tag{10}$$

The second term ($\mathrm{Term}_{i,2}$) accounts for the normal load effect as

$$\mathrm{Term}_{i,2} = \sin\left(2\arctan\left(\frac{F_{z,i}}{\left(a_{411}y_i^2 + a_{412}y_i + a_{413}\right)x_i + \left(a_{421}y_i^2 + a_{422}y_i + a_{423}\right)}\right)\right). \tag{11}$$

The third term ($\mathrm{Term}_{i,3}$) is a temperature scaling factor as

$$\mathrm{Term}_{i,3} = \left(b_{11}z_i^2 + b_{12}z_i + b_{13}\right). \tag{12}$$

The total cornering stiffness (BCD) is the product of these terms (Eq. (13)):

$$(BCD)_i = \mathrm{Term}_{i,1}\,\mathrm{Term}_{i,2}\,\mathrm{Term}_{i,3}. \tag{13}$$

The stiffness factor ($B_{y,i}$) is (Eq. (14)):

$$B_{y,i} = \frac{(BCD)_i}{C_y\,D_i}, \tag{14}$$

where C_y is the shape factor, and D_i is the peak lateral force (defined below).

Peak Lateral Force The peak lateral force (D_i) represents the maximum force the tire can generate, calculated as (Eq. (15)):

$$D_i = \mu_{y,\max,i}\,F_{z,i}. \tag{15}$$

Lateral Tire Force The lateral tire force ($F_{y,i}$) is computed using the following formula, a nonlinear function of the slip angle:

$$F_{y,i}(\alpha_i) = D_i \sin\left[C_y \tan^{-1}\left(B_{y,i}\alpha_i - E_y\left(B_{y,i}\alpha_i - \tan^{-1}(B_{y,i}\alpha_i)\right)\right)\right] + S_{vy,i}, \tag{16}$$

where E_y is the Curvature factor, and $S_{vy,i}$ is the Vertical shift.

To improve modeling accuracy under varying operating conditions, the traditional Pacejka magic-formula has been extended to include correction factors that account for temperature, tread depth, and inflation pressure effects on tire behavior. As demonstrated by Singh and Sivaramakrishnan [17], these parameters directly influence the tire's cornering stiffness and peak friction coefficient, which determine lateral force generation during aggressive maneuvers. Higher temperature or reduced tread depth tends to soften the tire compound, lowering stiffness and decreasing the attainable peak grip, whereas moderate increases in inflation pressure enhance stiffness but reduce the effective contact patch, leading to earlier saturation of the lateral force curve. Table 2 lists the variables used in the tire model and their values. All values for the rear tire are the same as the front tire.

Table 2: Tire model values and parameters

Parameter	Value	Unit	Description
x_f	32	psi	Front tire pressure
y_f	0.8	–	Front tread depth (dimensionless)
z_f	40	°C	Front tire surface temperature
x_r	32	psi	Rear tire pressure
y_r	0.8	–	Rear tread depth (dimensionless)
z_r	40	°C	Rear tire surface temperature
$\mu_{\max,f_0}$	1.0	–	Nominal peak grip coefficient (front tire)
a_{311}	30	$\frac{\mathrm{N}}{\mathrm{rad}\cdot\mathrm{psi}^2}$	Pacejka coefficient (front tire)
a_{312}	1000	$\frac{\mathrm{N}}{\mathrm{rad}\cdot\mathrm{psi}^2}$	Pacejka coefficient (front tire)
a_{313}	500	$\frac{\mathrm{N}}{\mathrm{rad}\cdot\mathrm{psi}^2}$	Pacejka coefficient (front tire)
a_{321}	200	$\frac{\mathrm{N}}{\mathrm{rad}\cdot\mathrm{psi}}$	Pacejka coefficient (front tire)
a_{322}	1000	$\frac{\mathrm{N}}{\mathrm{rad}\cdot\mathrm{psi}}$	Pacejka coefficient (front tire)
a_{323}	400	$\frac{\mathrm{N}}{\mathrm{rad}\cdot\mathrm{psi}}$	Pacejka coefficient (front tire)
a_{331}	150	$\frac{\mathrm{N}}{\mathrm{rad}}$	Pacejka coefficient (front tire)
a_{332}	100	$\frac{\mathrm{N}}{\mathrm{rad}}$	Pacejka coefficient (front tire)
a_{333}	800	$\frac{\mathrm{N}}{\mathrm{rad}}$	Pacejka coefficient (front tire)
a_{411}	500	$\frac{\mathrm{N}}{\mathrm{psi}}$	Pacejka coefficient (front tire)
a_{412}	200	$\frac{\mathrm{N}}{\mathrm{psi}}$	Pacejka coefficient (front tire)
a_{413}	1000	$\frac{\mathrm{N}}{\mathrm{psi}}$	Pacejka coefficient (front tire)
a_{421}	400	N	Pacejka coefficient (front tire)
a_{422}	150	N	Pacejka coefficient (front tire)
a_{423}	800	N	Pacejka coefficient (front tire)
b_{11}	0.0001	$^\circ\mathrm{C}^{-2}$	Temperature polynomial coefficient (front tire)
b_{12}	0.002	$^\circ\mathrm{C}^{-1}$	Temperature polynomial coefficient (front tire)
b_{13}	1.0	–	Temperature polynomial coefficient (front tire)

3 Optimized fuzzy controller design

3.1 Controller structure

Lotfi Zadeh first proposed the fuzzy logic [22], a nonlinear scheme expressly designed to accommodate model uncertainties. Because any mathematical representation of a real-world system necessarily omits or approximates certain parameters, uncertainty is inherently present in every model. For this reason, fuzzy control has emerged as a particularly

attractive strategy for autonomous-vehicle applications.

The control structure consists of two fuzzy-logic controllers acting on the nonlinear vehicle model described in Section 2. The first controller regulates lateral motion through the steering angle δ (FLC_δ), while the second controller governs longitudinal motion through the acceleration command a_x (FLC_{a_x}). Both controllers are of the Mamdani type and operate at each sampling instant using measurable states of the vehicle.

The lateral controller computes the steering command according to Eq. (17).

$$\delta = \mathcal{F}_\delta \left(e_y,\, e_\psi,\, \alpha_r \right). \tag{17}$$

These signals are derived from the vehicle's lateral–yaw dynamics given by Eqs. (4)–(16). The controller output δ directly influences the lateral tire forces $F_{y,f}$ and $F_{y,r}$ in the single-track model (Section 2), thus determining the vehicle's heading and lateral stability. Each input is described by three Gaussian membership functions. The Cartesian product of these inputs yields $3^3 = 27$ fuzzy rules, which are enumerated in Table 3.

The longitudinal controller determines the acceleration input as Eq. (18).

$$a_x = \mathcal{F}_{a_x} \left(e_{v_x},\, D_F,\, D_R \right). \tag{18}$$

Where D_F and D_R denote the distances to the front and rear surrounding vehicles, respectively. The distance variables are obtained from the traffic-scenario model, while the longitudinal acceleration a_x acts on the model's longitudinal dynamics through the driving force $F_{x,f} = ma_x$ (see Eq. (3)).

Each fuzzy controller establishes an explicit mapping between measurable vehicle states and corresponding control actions, allowing the nonlinear vehicle model and the fuzzy decision logic to operate in a closed loop.

The subsequent subsection defines the parameterization of these fuzzy controllers, including membership functions, rule bases, and scaling factors used for optimization.

Fig. 2 shows the closed-loop block diagram of the system. As can be seen, two fuzzy controllers are used to control longitudinal acceleration and lateral motion.

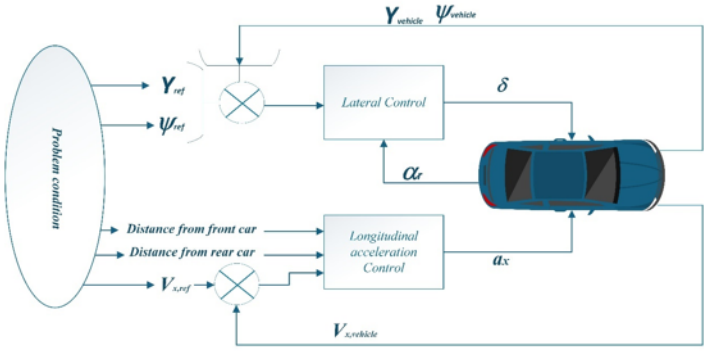

Figure 2: Closed-loop control diagram.

The rule base employs the following linguistic labels:

- N (Negative), Z (Zero), P (Positive)
- S (Small), L (Large)
- NB (Negative Big), NM (Negative Medium), NS (Negative Small)
- ZE (Zero, emphasizing negligible error)
- PB (Positive Big), PM (Positive Medium), PS (Positive Small)

These terms enable the controller to translate continuous sensor measurements into discrete inferences, facilitating appropriate corrective actions during complex maneuvers such as lane changes. As a result, the system maintains both tracking accuracy and safety under dynamically varying traffic conditions.

The longitudinal-acceleration controller employs three input variables-reference speed error e_{vx}, front-vehicle distance D_F, and rear-vehicle distance D_R. Each input is fuzzified using three Gaussian membership functions, yielding a $3^3 = 27$-rule inference base (see Table 4).

Table 3: Fuzzy controller rules for steering angle

e_y	N	N	N	N	N	N	N	N	N	Z	Z	Z	Z	Z	Z	Z	Z	Z	P	P	P	P	P	P	P	P	P
e_ψ	N	N	N	Z	Z	Z	P	P	P	N	N	N	Z	Z	Z	P	P	P	N	N	N	Z	Z	Z	P	P	P
α_r	N	Z	P	N	Z	P	N	Z	P	N	Z	P	N	Z	P	N	Z	P	N	Z	P	N	Z	P	N	Z	P
	↓	↓	↓	↓	↓	↓	↓	↓	↓	↓	↓	↓	↓	↓	↓	↓	↓	↓	↓	↓	↓	↓	↓	↓	↓	↓	↓
δ	NB	NM	NS	NM	NS	ZE	NS	ZE	PS	NM	NS	ZE	NS	ZE	PS	ZE	PS	PM	NS	ZE	PS	ZE	PS	PM	PS	PM	PB

Table 4: Fuzzy controller rules for longitudinal acceleration

e_{vx}	N	N	N	N	N	N	N	N	N	Z	Z	Z	Z	Z	Z	Z	Z	Z	P	P	P	P	P	P	P	P	P
D_F	S	S	S	Z	Z	Z	L	L	L	S	S	S	Z	Z	Z	L	L	L	S	S	S	Z	Z	Z	L	L	L
D_R	S	Z	L	S	Z	L	S	Z	L	S	Z	L	S	Z	L	S	Z	L	S	Z	L	S	Z	L	S	Z	L
	↓	↓	↓	↓	↓	↓	↓	↓	↓	↓	↓	↓	↓	↓	↓	↓	↓	↓	↓	↓	↓	↓	↓	↓	↓	↓	↓
a_x	NS	NM	NL	NS	NM	NL	NS	NM	NL	NS	NS	NS	NS	NS	NS	NS	NS	NS	NS	NS	NS	NS	ZE	ZE	ZE	PS	PS	PS

To implement the fuzzy controller, a singleton fuzzifier is used, which is written in Eq. (19). The singleton fuzzifier $\mu_{A'}$ assigns a membership value of 1 to the input when X equals the setpoint X^*, and 0 otherwise, providing a simple and efficient mechanism for implementing the fuzzy controller.

$$\mu_{A'}(X) = \begin{cases} 1, & X = X^*, \\ 0, & \text{otherwise.} \end{cases} \tag{19}$$

For the inference engine, the minimum Mamdani is used, as written in Eq. (20).

$$\mu_{B'}(y) = \max_{l=1,\ldots,M} \left[\sup_{x \in U} \min \left(\mu_{A'}(x),\, \mu_{A_1^l}(x),\, \ldots,\, \mu_{A_n^l}(x),\, \mu_{B^l}(y) \right) \right]. \tag{20}$$

where $\mu_{B'}(y)$ is the aggregated fuzzy output membership function, $\mu_{A_i^l}(x)$ represents the input membership functions for the i-th (Three inputs are used to control the steering angle, and three input variables are used to control the longitudinal acceleration) input of the l-th rule, $\mu_{B^l}(y)$ denotes the output membership function for the l-th rule, M is the total number of rules, $x \in U$ indicates the input universe. Given that the membership functions are in the range -1 to 1, the inputs of the fuzzy controller are also in the range -1 and 1. For this purpose, a nonlinear mapping is used, which is written as

$$x_i^{new} = 2 \left(\frac{1}{1 + e^{-0.5 x_i}} \right) - 1. \tag{21}$$

After mapping the input-output state space variables to the range of -1 to 1, the output of the mapping, represented by x_i^{new}, is considered as the controller input. The de-fuzzifier used is the centroid, which is written as follows

$$y^* = \frac{\sum_{i=1}^{m} \overline{y}^{(i)} w_i}{\sum_{i=1}^{m} w_i}. \tag{22}$$

y^* represents discrete output values, w_i signifies the weights derived from rule firing strengths, and $\overline{y}^{(i)}$ represents the center of each membership function. According to Eqs. (19), (20), and (22) being Gaussian, the input and output membership functions of Eq. (23) are written.

$$\begin{cases} \delta = \dfrac{\sum_{l_1=1}^{m_1} \left(\min_{i_1=1,\ldots,n_1} \left(\exp\left(-\left(\frac{x_{i_1}^{new} - c_{i_1}^{l_1}}{\sigma_{i_1}^{l_1}} \right)^2 \right), \exp\left(-\left(\frac{y_1 - d_1^{l_1}}{\theta_1^{l_1}} \right)^2 \right) \right) \right) \overline{y}^{(l_1)}}{\sum_{l_1=1}^{m_1} \left(\min_{i_1=1,\ldots,n_1} \left(\exp\left(-\left(\frac{x_{i_1}^{new} - c_{i_1}^{l_1}}{\sigma_{i_1}^{l_1}} \right)^2 \right), \exp\left(-\left(\frac{y_1 - d_1^{l_1}}{\theta_1^{l_1}} \right)^2 \right) \right) \right)} \\ a_x = \dfrac{\sum_{l_2=1}^{m_2} \left(\min_{i_2=1,\ldots,n_2} \left(\exp\left(-\left(\frac{x_{i_2}^{new} - c_{i_2}^{l_2}}{\sigma_{i_2}^{l_2}} \right)^2 \right), \exp\left(-\left(\frac{y_2 - d_2^{l_2}}{\theta_2^{l_2}} \right)^2 \right) \right) \right) \overline{y}^{(l_2)}}{\sum_{l_2=1}^{m_2} \left(\min_{i_2=1,\ldots,n_2} \left(\exp\left(-\left(\frac{x_{i_2}^{new} - c_{i_2}^{l_2}}{\sigma_{i_2}^{l_2}} \right)^2 \right), \exp\left(-\left(\frac{y_2 - d_2^{l_2}}{\theta_2^{l_2}} \right)^2 \right) \right) \right)} \end{cases} \tag{23}$$

$n_k (k = 1, 2)$ is the number of input variables, and x_{ik}^{new} denotes the i-th input variable, and m_k is the number of rules. There is no general mathematical proof that a specific membership function type is universally optimal for fuzzy control systems, and the selection is often based on empirical analysis and system-specific performance. Recent comparative studies confirm that Gaussian membership functions provide smooth, differentiable transitions between fuzzy regions and yield superior dynamic performance compared with triangular or trapezoidal alternatives [15].

Fig. 3 is plotted for a better understanding of the optimized parameters. As can be seen, two parameters, the center of the Gaussian function and its skewness, are optimized.

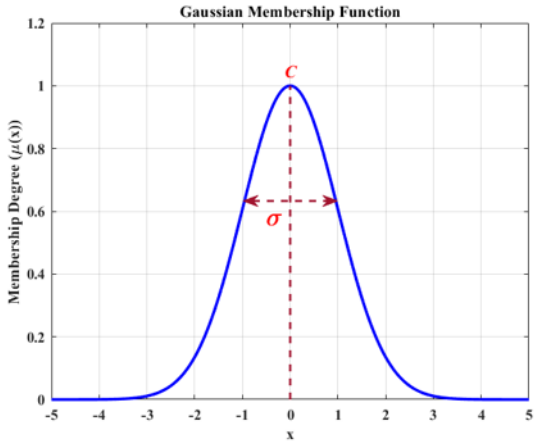

Figure 3: Parameters of Gaussian membership functions.

3.2 Optimization algorithm (slime mould algorithm)

The Slime Mould Algorithm is a population-based metaheuristic inspired by oscillatory search and foraging behavior of the *Physarum polycephalum* organism [7].

At each iteration, a population of N_p candidate solutions-referred to as agents-explores the search space. The fitness of each agent corresponds to the evaluated cost $J_{\text{Base}}(\Theta)$ obtained from simulation of the closed-loop vehicle–controller system. Agents with lower cost values represent stronger slime mould individuals and exert a greater influence on the population update.

The position of each agent is updated using adaptive weights that balance exploration and exploitation. During early iterations, larger weights encourage global exploration of the parameter space, while subsequent iterations gradually intensify local exploitation around promising regions. A stochastic phase is also included to prevent premature convergence. The general update rule can be expressed as:

$$\Theta_i^{(t+1)} = \begin{cases} \Theta_{\text{best}}^{(t)} + p\Big(\omega_i\, r_1 \bigodot (\Theta_A^{(t)} - \Theta_B^{(t)})\Big), & \text{if } r_2 < z, \\ r_3 \bigodot (\Theta_U - \Theta_L) + \Theta_L, & \text{otherwise,} \end{cases} \tag{24}$$

where $\Theta_i^{(t)}$ is the i^{th} agent at iteration t, $\Theta_{\text{best}}^{(t)}$ denotes the current best solution, r_1, r_2, r_3 are random vectors/scalars in $[0, 1]$, ω_i is the fitness-dependent weight of the agent, p is a control parameter regulating step amplitude, and Θ_U, Θ_L are the upper and lower parameter bounds, respectively. The operator $\bigodot$ denotes element-wise multiplication, and $\Theta_A^{(t)}$, $\Theta_B^{(t)}$ are two randomly selected agents at iteration t. The probabilistic switch governed by r_2 and threshold z controls the transition between exploitation and exploration phases.

The iterative process continues until either the maximum iteration number $T_{\max}$ is reached or the variation of the best fitness value falls below a predefined tolerance. The final parameter vector $\Theta^\star$ defines the tuned fuzzy controllers subsequently employed in the lane-change simulations described in Section 4.

3.3 Optimization problem formulation and cost function

The fuzzy-logic controllers include multiple parameters for membership functions: centers $(c_i^l,\ d_i^l)$, standard deviations $(\sigma_i^l,\ \theta_i^l)$ as well as rule weights that strongly influence control performance. These parameters are collectively represented by the vector $\Theta \in \mathbb{R}^{n_\Theta}$, where $n_\Theta = 81$ in the present design.

The controller tuning is formulated as a constrained simulation-based optimization problem. For each candidate Θ, the nonlinear vehicle model in Section 2 is simulated in closed loop over the lane-change horizon $t \in [0, t_f]$, producing the tracking errors and control inputs, and a scalar performance index $J_{\text{obj}}(\Theta)$ is computed. The optimal controller parameters are obtained by solving

$$\begin{aligned} \Theta^\star &= \arg\min_{\Theta} J_{\text{obj}}(\Theta) \\ \text{s.t.} \quad \Theta_L &\le \Theta \le \Theta_U, \\ |\delta(t;\Theta)| &\le \delta_{\max}, \\ |a_x(t;\Theta)| &\le a_{x,\max}, \\ 0 \le v_x(t;\Theta) &\le 20\ \frac{\text{m}}{\text{s}}, \\ D_{\text{col}}(t;\Theta) &\ge 0 \qquad \forall t \in [0,\ t_f]\,. \end{aligned} \tag{25}$$

In (25), $\delta(t;\Theta)$ and $a_x(t;\Theta)$ are the steering and longitudinal acceleration commands produced by the fuzzy controllers (Eqs. (17)–(18)) and applied to the nonlinear vehicle model in Section 2. Therefore, the constraints are evaluated along the entire closed-loop simulation horizon $[0,\ t_f]$.

Safety-margin definitions To avoid ambiguity between collision avoidance and conservative clearance, we distinguish a hard collision-avoidance margin from an additional buffer margin. Let $d_{\text{Euc},j}(t)$ denote the Euclidean distance between the ego vehicle and the j-th surrounding vehicle in the traffic scenario. We define

$$d_{\text{Euc},j}(t) = \sqrt{\left(y(t) - y_j(t)\right)^2 + \left(s(t) - s_j(t)\right)^2}, \qquad j = 1, \ldots, 4. \tag{26}$$

Hard collision-avoidance margin We define

$$D_{\text{col}}(t;\Theta) = \min_{j \in \mathcal{N}(t)} \left(d_{\text{Euc},j}(t) - w_{\updownarrow}\right), \tag{27}$$

where $w_{\updownarrow}$ represents the collision envelope (minimum clearance). In the implementation, $w_{\updownarrow}$ is selected conservatively as

$$w_{\updownarrow} = w_{\text{veh}} + \Delta w, \qquad w_{\text{veh}} = 1.8 \text{ m}, \qquad \Delta w = 0.2 \text{ m}. \tag{28}$$

The hard safety constraint in (25) is $D_{\text{col}}(t;\Theta) \ge 0$ for all $t \in [0,\ t_f]$, which guarantees collision-free operation.

Conservative buffer margin (implementation-aligned) In addition, we define a conservative buffer margin that includes an extra clearance offset $d_0 > 0$ (in our simulations $d_0 = 5$ m). Since this buffer is meaningful mainly when a surrounding vehicle is laterally close to the ego vehicle (same-lane / cut-in / merge region), we define the conflict-active neighbor set

$$\mathcal{N}_{\text{conf}}(t) = \left\{ j \in \{1, \ldots, 4\} : |y(t) - y_j(t)| \le y_{\text{conflict}} \right\},$$

where $y_{\text{conflict}} = \frac{1}{2} w_{\text{lane}}$ in this study. The buffer margin is then defined as

$$D_{\text{buf}}(t;\Theta) = \min_{j \in \mathcal{N}_{\text{conf}}(t)} \left(d_{\text{Euc},j}(t) - \left(w_{\updownarrow} + d_0\right)\right). \tag{29}$$

If $\mathcal{N}_{\text{conf}}(t) = \varnothing$, the buffer margin is considered not active and is omitted from minimum computations. The buffer margin is used for robust assessment and reporting (and may be partially consumed), while collision avoidance is ensured by $D_{\text{col}}(t;\Theta) \ge 0$.

Finally, the SMA is used as a numerical solver for the above constrained minimization: each SMA agent encodes one candidate parameter vector Θ, its fitness is the simulation-based value $J_{\text{obj}}(\Theta)$, constraints are enforced during evaluation (and/or via penalization of infeasible solutions), and the best agent at termination yields $\Theta^\star$, i.e., the final tuned fuzzy-controller parameters used in Section 4. The objective function $J_{\text{obj}}(\Theta)$ is defined below (see Eq. (32)) as a weighted baseline tracking/control-effort index augmented with a Lyapunov-based stability penalty.

Note that θ_i^l denotes a membership-function spread and should not be confused with the decision vector Θ.

The rule firing strength is computed by the minimum Mamdani operator as

$$w_l = \min_{i=1,\ldots,n} \left(\exp\left(-\left(\frac{x_i^{new} - c_i}{\sigma_i} \right)^2 \right), \exp\left(-\left(\frac{y - d}{\theta} \right)^2 \right) \right). \tag{30}$$

Given that c_i, σ_i, d, and θ change with the optimization process, the value of w_l also changes indirectly and the optimization process is carried out in such a way that the set of points representing c_i, σ_i, d, and θ enter the controller function and membership functions are built. Hence, it is said that the weights of the rules are optimized simultaneously and indirectly. Now, to solve this problem, we consider a new weight in the range of 0 to 1 for each rule, and we use the optimization algorithm to find these new weights. The new equation obtained is shown in Eq. (31). In fact, this equation is obtained from Eq. (23). By doing this, we can remove the created limitations and by adding a new variable, we will have a better ability to control.

$$\begin{cases} \delta = \dfrac{\sum_{l_1=1}^{m_1}\left(\min_{i_1=1,\ldots,n_1}\left(\exp\left(-\left(\frac{x_{i_1}^{new}-c_{i_1}^{l_1}}{\sigma_{i_1}^{l_1}}\right)^2\right),\exp\left(-\left(\frac{y_1-d_1^{l_1}}{\theta_1^{l_1}}\right)^2\right)\right)\right)\overline{y}^{(l_1)}\, w_{l_1}^{\mathrm{opt}}}{\sum_{l_1=1}^{m_1}\left(\min_{i_1=1,\ldots,n_1}\left(\exp\left(-\left(\frac{x_{i_1}^{new}-c_{i_1}^{l_1}}{\sigma_{i_1}^{l_1}}\right)^2\right),\exp\left(-\left(\frac{y_1-d_1^{l_1}}{\theta_1^{l_1}}\right)^2\right)\right)\right) w_{l_1}^{\mathrm{opt}}} \\ a_x = \dfrac{\sum_{l_2=1}^{m_2}\left(\min_{i_2=1,\ldots,n_2}\left(\exp\left(-\left(\frac{x_{i_2}^{new}-c_{i_2}^{l_2}}{\sigma_{i_2}^{l_2}}\right)^2\right),\exp\left(-\left(\frac{y_2-d_2^{l_2}}{\theta_2^{l_2}}\right)^2\right)\right)\right)\overline{y}^{(l_2)}\, w_{l_2}^{\mathrm{opt}}}{\sum_{l_2=1}^{m_2}\left(\min_{i_2=1,\ldots,n_2}\left(\exp\left(-\left(\frac{x_{i_2}^{new}-c_{i_2}^{l_2}}{\sigma_{i_2}^{l_2}}\right)^2\right),\exp\left(-\left(\frac{y_2-d_2^{l_2}}{\theta_2^{l_2}}\right)^2\right)\right)\right) w_{l_2}^{\mathrm{opt}} \end{cases} \tag{31}$$

where $w_{l_k}^{\mathrm{opt}}$ represents the optimal weight of the l-th rule.

The optimal parameter set is obtained by minimizing a performance-index function that quantifies tracking accuracy and control smoothness. The cost function is written in Eq. (32).

$$J_{\mathrm{Base}}(\Theta) = \int_0^{t_f} \tau\left(w_{e_{vx}}\left|e_{vx}(\tau)\right| + w_{e_y}\left|e_y(\tau)\right| + w_{e_\psi}\left|e_\psi(\tau)\right| + w_u\left(\frac{|\delta(\tau)|}{\delta_{\max}} + \frac{|a_x(\tau)|}{a_{x,\max}}\right)\right) d\tau. \tag{32}$$

The first three terms penalize longitudinal-speed, lateral-position, and yaw-angle errors, while the last two terms limit excessive steering and acceleration commands. Using separate penalties enables the optimizer to balance lateral stability and longitudinal comfort without biasing one control channel over the other.

The optimization is subject to physical and safety constraints:

$$\begin{aligned} |\delta(t)| &\le \delta_{\max}, \\ |a_x(t)| &\le a_{x,\max}, \\ 0 \le v_x(t) &\le 20\ \frac{\mathrm{m}}{\mathrm{s}}, \\ D_{\mathrm{col}}(t) &\ge 0. \end{aligned} \tag{33}$$

Each candidate parameter vector Θ defines a pair of fuzzy control laws that are simulated on the nonlinear vehicle model of Section 2 to evaluate $J_{\mathrm{Base}}(\Theta)$. The search for the minimum of J_{Base} is carried out using the Slime Mould Algorithm, which iteratively updates the candidate solutions through adaptive exploration–exploitation rules.

3.4 Stability considerations

Although the nonlinear Mamdani-type fuzzy controllers do not admit a closed-form Lyapunov proof as in classical linear systems, the optimization stage integrates stability-related constraints to ensure bounded system responses.

Lyapunov-based penalty approach

Let the vehicle lateral–yaw and longitudinal tracking-error dynamics be described by the state vector

$$X = \left[e_y,\ e_\psi,\ e_{vx}\right]^T, \tag{34}$$

where e_y, e_ψ, and e_{vx} denote lateral-position, yaw-angle, and longitudinal-speed errors, respectively.

A quadratic Lyapunov candidate function is defined as

$$V(X) = X^T P X, \qquad P = P^T > 0. \tag{35}$$

For each candidate solution generated by the SMA during optimization, the time derivative of V is evaluated numerically along the simulated trajectories of the closed-loop system as

$$\dot{V} = \nabla V \cdot f_{\mathrm{cl}}(X), \tag{36}$$

where $f_{\mathrm{cl}}(X)$ represents the nonlinear closed-loop vehicle dynamics.

A stability penalty is introduced into the cost function whenever

$$\dot{V} > -\varepsilon \|X\|^2, \tag{37}$$

with $\varepsilon > 0$ being a small constant. This condition ensures that the Lyapunov function decreases over time for sampled operating points, promoting asymptotic convergence of tracking errors and suppressing oscillations. Through this penalty mechanism, the optimization algorithm naturally prefers fuzzy-controller parameters that yield stable, well-damped responses without altering the Mamdani inference structure. To enforce the stability condition, the following cost function is used:

$$J_{\mathrm{Lyap}}(\Theta) = J_{\mathrm{Base}}(\Theta) + \omega_{\mathrm{Lyap}} \int_0^{t_f} \left\{ \max\left(0,\ \dot{V} + \varepsilon \|X\|^2\right) \right\}^2 d\tau, \tag{38}$$

where $\omega_{\mathrm{Lyap}} > 0$ is called the Lyapunov weight. This weight is greater than zero and when the condition in (37) is not satisfied, the cost function increases.

3.5 Robustness analysis

To formalize robustness, we model parametric uncertainty and unmodeled dynamics as a lumped bounded disturbance acting on the closed-loop error dynamics. The resulting closed-loop error dynamics can be expressed in lumped form as

$$\dot{X} = f(X) + d(t), \tag{39}$$

where $f(\bullet)$ denotes the nominal closed-loop error dynamics induced by the fuzzy controllers and the nominal vehicle model, and $d(t)$ captures the effects of uncertainty, external perturbations, and unmodeled dynamics.

Assumption (bounded disturbance). There exists a constant $\overline{d}$ such that

$$\|d(t)\| < \overline{d} \qquad \forall t \geq 0. \tag{40}$$

Consider the candidate Lyapunov function

$$V(X) = \frac{1}{2} X^T X. \tag{41}$$

Differentiating (41) and using (39) yields

$$\dot{V}(X) = X^T f(X) + X^T d(t). \tag{42}$$

In the nominal case ($d \equiv 0$), the tuning procedure includes a Lyapunov-inspired penalty that discourages non-dissipative behavior and promotes a local dissipation condition of the form

$$X^T f(X) \leq -c \|X\|^2, \tag{43}$$

for some constant ($c > 0$) in a neighborhood of the origin. Using (43) and $X^T d(t) \leq \|X\| \ \|d(t)\|$ we obtain

$$\dot{V}(X) \leq -c \|X\|^2 + \|X\| \ \overline{d}. \tag{44}$$

Applying $ab \leq \frac{c}{2} a^2 + \frac{1}{2c} b^2$ yields

$$\|X\| \ \overline{d} \leq \frac{c}{2} \|X\|^2 + \frac{1}{2c} \overline{d}^2. \tag{45}$$

This implies that

$$\dot{V}(X) \leq -\frac{c}{2} \|X\|^2 + \frac{1}{2c} \overline{d}^2. \tag{46}$$

Therefore, the tracking error $X(t)$ is uniformly ultimately bounded (UUB): it enters and remains in the compact set

$$\mathcal{B} = \left\{ X \in \mathbb{R}^3 : \|X\| \leq \frac{\overline{d}}{c} \right\}. \tag{47}$$

This provides a mathematical robust statement: under bounded uncertainty/disturbance, the proposed controller guarantees bounded tracking errors. In addition, the imposed actuator limits on steering and longitudinal acceleration ensure bounded control actions during operation.

4 Simulation results

Fig. 4 illustrates the primary test scenario, in which an autonomous vehicle navigates a three-lane roadway. Beginning in lane 3, the vehicle executes a controlled lane change to lane 1 while avoiding collisions with neighboring traffic. After maintaining its trajectory in lane 1 for a designated interval, the vehicle then shifts into lane 2.

Throughout these maneuvers, longitudinal speed is adaptively regulated to preserve a safe following distance. Whenever the gap to the preceding vehicle exceeds the safety threshold, the controller accelerates up to the 20 $\frac{\text{m}}{\text{s}}$ limit. Conversely, as the inter-vehicle distance approaches the minimum safe margin, speed is reduced to match that of the lead vehicle. This combined strategy of adaptive acceleration and precise steering enables smooth, stable lane changes and robust performance under dynamic traffic conditions.

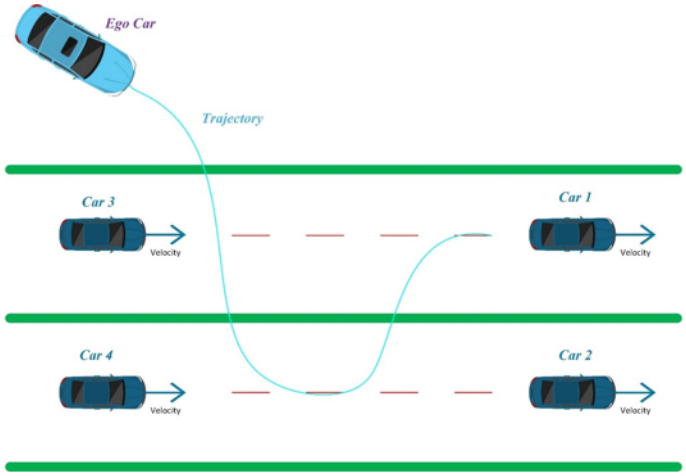

Figure 4: Autonomous car travel path.

Also, in Table 5, the specifications of the vehicle parameters used can be seen.

Table 5: Vehicle parameters used in simulations

Parameter	Value	Unit	Description
m	1500	kg	Vehicle mass
I_Z	3000	$\text{kg} \cdot \text{m}^2$	Yaw moment of inertia
l_f	1.2	m	Distance from CoG to front axle
l_r	1.5	m	Distance from CoG to rear axle
h	0.5	m	CoG height
ρ	1.225	kg/m^3	Air density
C_d	0.3	–	Drag coefficient
A_f	2.2	m^2	Frontal area
g	9.81	m/s^2	Gravitational acceleration

In Fig. 5(a), the vehicle's lateral position is plotted against its longitudinal travel over roughly 450 m. The trajectory begins at the initial point (green marker) and ends at the final point (red marker), with the path remaining within the lane boundaries. Fig. 5(b) charts the yaw angle versus longitudinal distance, showing a peak near 225 m that corresponds to the vehicle's orientation adjustment during the lane change. Fig. 5(c) presents the path curvature, which quantifies the instantaneous rate of change in heading and highlights the sharpness of the bend at the maneuver's apex.

Fig. 6 compares the input membership functions before and after optimization. Panel (a) displays the optimized Gaussian membership functions, while panel (b) shows the original, unoptimized functions-demonstrating clear shifts in the centroids and spreads following the tuning process. Similarly, Fig. 7(a) and Fig. 7(b) depict the optimized and unoptimized output membership functions, respectively, illustrating analogous positional changes that result from the optimization.

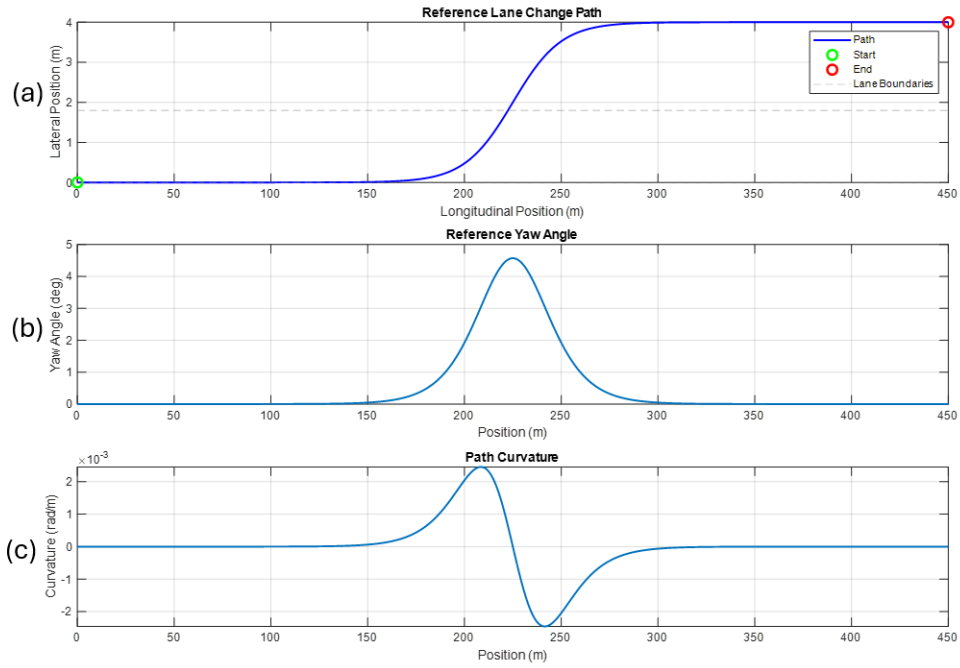

Figure 5: Autonomous vehicle route details: (a) lateral position, (b) yaw angle, and (c) path curvature.

Fig. 8(a) presents the vehicle's lateral displacement relative to the reference trajectory (red dashed line). Beginning with a 1 m offset, the optimized fuzzy controller (blue line) realigns the vehicle to the desired path within a short interval, whereas the unoptimized Type-1 controller (black dashed line) exhibits pronounced oscillations, indicating inferior lateral control.

Fig. 8(b) shows longitudinal velocity under both control schemes. From an initial 12 $\frac{\text{m}}{\text{s}}$, the vehicle accelerates to the 20 $\frac{\text{m}}{\text{s}}$ setpoint when no leading vehicle is within the safety threshold and decelerates to match the speed of a preceding vehicle as the gap narrows. Despite imposed speed variations in the lead vehicle, the optimized controller tracks the reference speed with negligible error, while the unoptimized controller displays minor deviations.

Fig. 8(c) compares yaw-rate responses during the lane-change maneuver. The optimized controller produces a distinct initial peak followed by rapid damping, whereas the unoptimized controller sustains large oscillations, revealing poorer yaw-rate regulation.

Fig. 8(d) depicts steering-angle dynamics, highlighting a peak at approximately 15 s corresponding to the lane-change initiation. The optimized controller quickly returns the steering angle to zero after the maneuver, while the unoptimized controller requires a longer settling time.

Fig. 8(e) plots lateral-position error, which starts at -1 m. The optimized controller reduces this error to near zero in about 2 s, with only minor fluctuations during each lane transition. By contrast, the unoptimized controller converges more slowly and exhibits larger transient errors.

Fig. 8(f) illustrates longitudinal-velocity error under both controllers. The optimized controller corrects an initial error of roughly 5 $\frac{\text{m}}{\text{s}}$ to near zero within seconds, outperforming the unoptimized controller in both convergence speed and steadiness.

Collectively, these results demonstrate that the optimized fuzzy controller delivers superior trajectory-tracking performance-minimizing lateral and longitudinal errors and ensuring rapid stabilization during complex lane changes-thereby confirming its robustness under dynamic driving conditions.

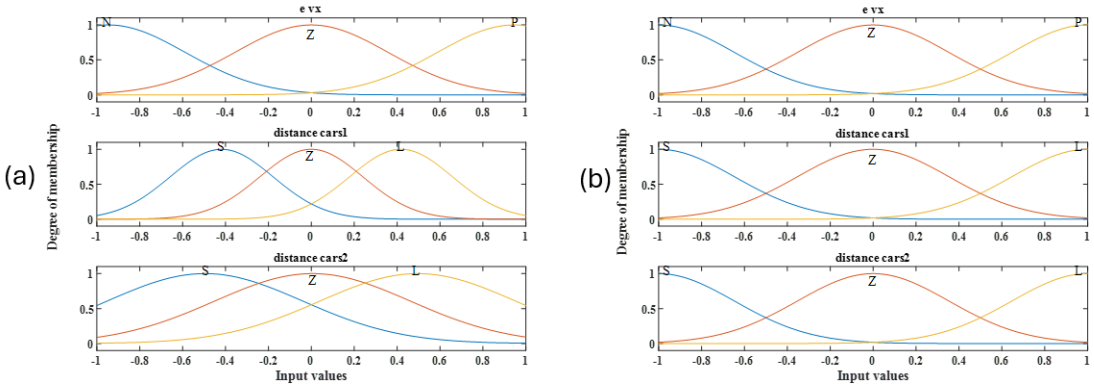

Figure 6: Input membership functions: optimized vs. unoptimized.

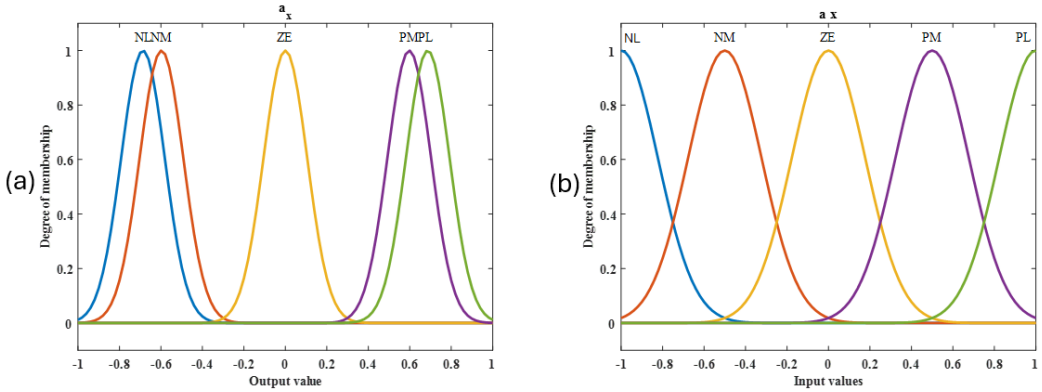

Figure 7: Output membership functions: optimized vs. unoptimized.

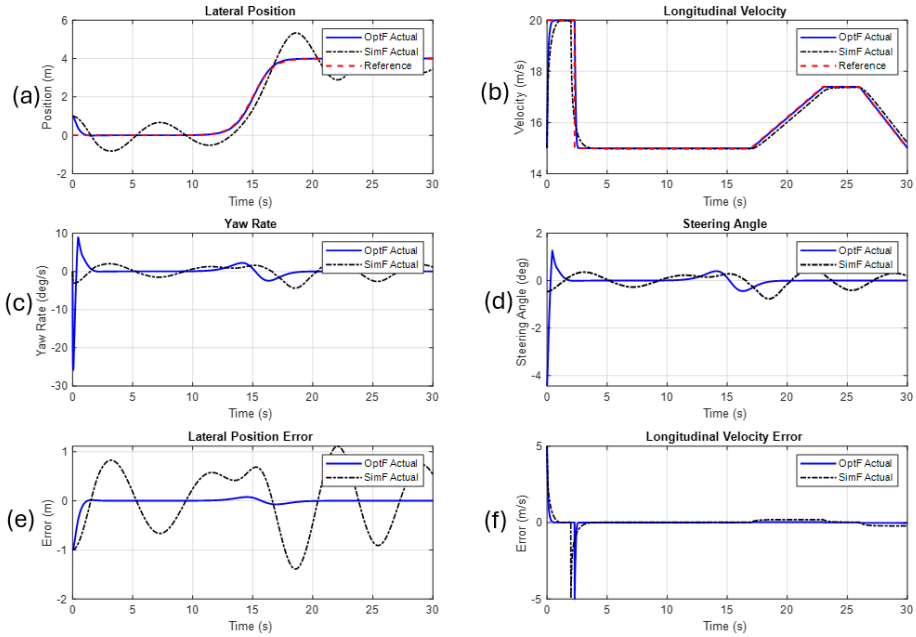

Figure 8: Optimized and unoptimized controller performance comparison: (a) lateral position, (b) longitudinal speed, (c) yaw rate, (d) steering angle, (e) lateral position error, and (f) longitudinal velocity error.

Fig. 9(a) shows the speeds of five simulated cars (one under control and four for testing our controllers). As seen in the scenario, two cars have a constant speed, and one car has a variable speed. As mentioned, as the speed of the car in front changes, the speed of the autonomous car also changes (this change is so that the safety distance is always maintained; however, the car under control has a maximum speed of 20 $\frac{\mathrm{m}}{\mathrm{s}}$). Fig. 9(b) shows the acceleration of the autonomous car, and as seen, if the speed of the car in front increases, our car will accelerate. Fig. 9(c) illustrates the collision-avoidance margin $D_{\mathrm{col}} = d_{\mathrm{Euc}} - w_{\updownarrow}$. As observed, D_{col} does not become negative during the maneuver, indicating collision-free behavior. A more conservative buffer margin $D_{\mathrm{buf}} = d_{\mathrm{Euc}} - \left(w_{\updownarrow} + d_0\right)$ is analyzed separately in the Monte-Carlo robustness study.

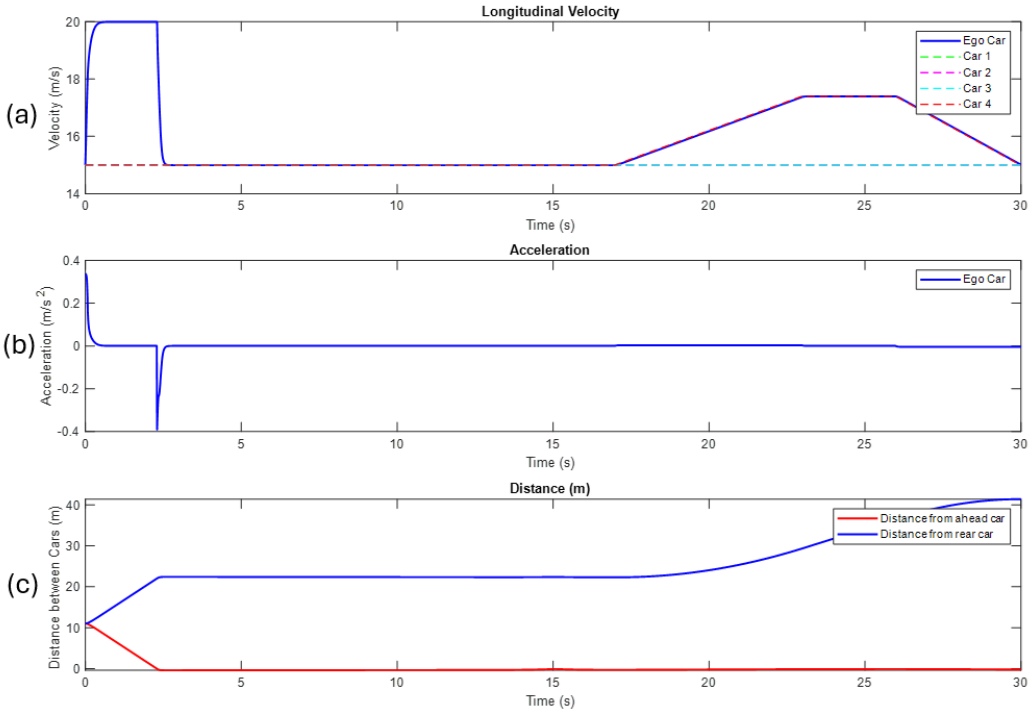

Figure 9: Performance evaluation of two fuzzy controllers: (a) velocity tracking, (b) longitudinal acceleration produced, (c) safety margin defined by the difference between the Euclidean distance and the collision envelope.

Fig. 10(a–c) shows the fuzzy controller surface FLC_{a_x}, and Fig. 10(d–f) shows the fuzzy controller surface FLC_{δ}. In general, fuzzy surface diagrams display output values relative to input variables. These shapes can be explained according to the rules mentioned. The distance_car1 axes represent the distance of the ego car from the car in front in the lane where the car is located, and the distance_car2 axis represents the distance of the ego car from the car behind in the specified lane. As illustrated in Fig. 10(a), the longitudinal acceleration of the controlled vehicle decreases as the distance to the leading vehicle decreases, and conversely, increases as the distance increases. A similar relationship can be observed in other cases as well. All simulation codes, parameters, and implementation files used in this study are publicly available at the following repository: CODE EXPLANATION AND SIMULATION RESULTS, allowing full reproducibility of the reported results.

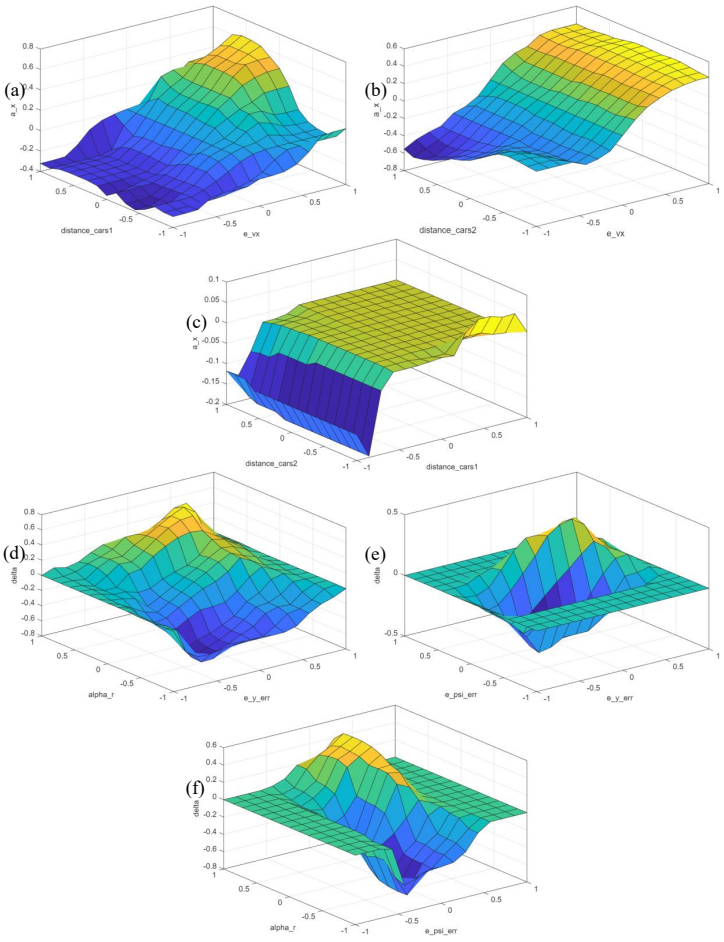

Figure 10: Controller surfaces: (a–c) FLC_{a_x} and (d–f) FLC_{δ}.

4.1 Monte-Carlo robustness validation

To assess the robustness of the proposed controller against modeling uncertainties and implementation imperfections, a Monte-Carlo study with $N = 20$ trials is performed. In all trials, the tuned controller parameter vector $\Theta^{\star}$ is kept fixed (i.e., no re-optimization is carried out), and the closed-loop lane-change simulation is repeated under randomized perturbations.

Uncertainty and perturbation model In each trial, the following uncertainty sources are applied:

(*i*) mass uncertainty: the vehicle mass m is perturbed within $\pm 10\%$ of its nominal value.

(*ii*) yaw-inertia uncertainty: the yaw moment of inertia I_Z is perturbed within $\pm 10\%$.

(*iii*) road friction uncertainty: the road friction coefficient μ is sampled uniformly within $[0.60,\ 1.00]$.

(*iv*) tire-parameter uncertainty: tire-related parameters are perturbed within $\pm 15\%$ to emulate variations due to pressure, temperature, and wear.

Moreover, two implementation imperfections are enabled:

(v) actuator transport delay: the steering and longitudinal-acceleration commands are delayed by a random value in $[0.05,\ 0.10]$ s, implemented via discrete-time command buffers.

(vi) measurement noise: additive Gaussian noise is injected into the measured lateral error e_y, heading error e_ψ, and longitudinal speed v_x (with the standard deviations specified in the simulation settings).

Reproducibility For each trial k, a deterministic random seed ($\text{Seed}_k = \text{Seed}_0 + k$) is assigned to the simulation run, ensuring repeatability of the injected measurement-noise and actuator-delay realizations.

Safety metrics and evaluation For each trial, we log the hard collision-avoidance margin $D_{\text{col}}(t;\Theta^\star)$ and the conservative buffer margin $D_{\text{buf}}(t;\Theta^\star)$. The hard margin D_{col} is evaluated at all time instants. In contrast, the buffer margin D_{buf} is evaluated only during conflict-active intervals (when $|y(t)-y_j(t)| \le y_{\text{conflict}}$ for at least one surrounding vehicle); if no vehicle is in the conflict region, the buffer metric is considered not active and is omitted from the minimum computations.

Each trial is summarized by the minimum margins

$$\min_t\ D_{\text{col}}\left(t;\Theta^\star\right), \qquad \min_t\ D_{\text{buf}}\left(t;\Theta^\star\right),$$

where $\min_t\ D_{\text{buf}}\left(t;\Theta^\star\right)$ is computed over conflict-active instants only. A collision violation is declared if $\min_t\ D_{\text{col}}\left(t;\Theta^\star\right) < -\varepsilon_{\text{col}}$, where $\varepsilon_{\text{col}} = 10^{-3}$ m is a small numerical tolerance introduced to avoid false violations caused by numerical noise. A buffer violation is declared if $\min_t\ D_{\text{buf}}\left(t;\Theta^\star\right) < 0$ during conflict-active intervals, indicating partial consumption of the conservative clearance offset d_0. Importantly, buffer violation does not imply collision as long as $D_{\text{col}}\left(t;\Theta^\star\right) \ge 0$ is maintained.

Fig. 11 reports the distribution of the minimum conservative buffer margin across the Monte-Carlo trials, showing how often (and by how much) the additional buffer d_0 is consumed under combined uncertainties, while the hard collision-avoidance constraint remains satisfied.

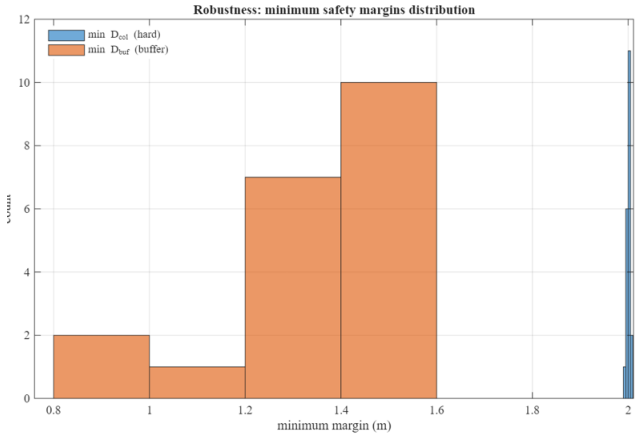

Figure 11: Robustness: minimum safety margin distribution across Monte-Carlo trials.

Fig. 11 reports robustness by showing the empirical distributions of the minimum safety margins across the Monte-Carlo trials. The distribution of $\min D_{\text{col}}$ (hard margin) is tightly concentrated near 2.0 m, meaning that even the worst-case trial retains a large positive hard clearance. This confirms that the hard collision-avoidance constraint is robustly satisfied within the uncertainty ranges considered.

In contrast, the distribution of the conservative buffer margin $\min D_{\text{buf}}$ is broader and spans approximately from 0.8 m to 1.6 m. Most trials cluster in the $[1.2,\ 1.6]$ m range, while a small number of trials reach values near $0.8-1.0$ m. Since D_{buf} includes the extra offset d_0 and is evaluated only during conflict-active intervals, these smaller values indicate that, in some realizations, the ego vehicle temporarily approaches the surrounding vehicles closely enough to consume a larger portion of the conservative buffer. Importantly, this does not imply collision because the hard margin D_{col} remains strongly positive throughout the trials, which is consistent with the separation between the hard safety metric and the conservative buffer metric adopted in the implementation.

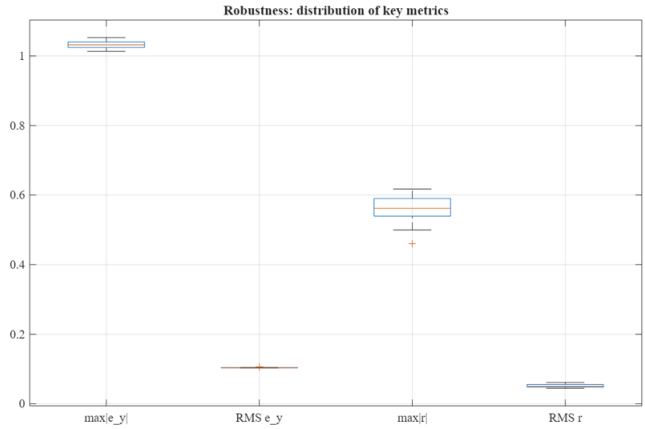

Figure 12: Robustness: boxplots of key closed-loop performance metrics across Monte-Carlo trials.

Fig. 12 illustrates the maximum absolute lateral error $\max|e_y|$ is tightly clustered around ≈ 1.03 m, with a narrow interquartile range (roughly $1.02 - 1.04$ m) and whiskers extending only slightly (approximately $1.01 - 1.06$ m). This indicates that the peak lateral deviation is highly repeatable and only weakly affected by the considered uncertainties.

The RMS lateral error is approximately $\mathrm{RMS}(e_y) \approx 0.10$ m, with an extremely small spread across trials (the box is nearly collapsed around 0.10 m), confirming that the typical tracking error remains consistently low even under perturbations.

Regarding yaw-rate behavior, the peak yaw rate $\max|r|$ has a median close to ≈ 0.56 rad/s, with moderate dispersion (IQR roughly $0.54 - 0.59$ rad/s and whiskers approximately $0.50 - 0.62$ rad/s). A low outlier is observed around ≈ 0.46 rad/s, which corresponds to a trial where the maneuver required less aggressive yaw dynamics. Finally, the yaw-rate RMS remains small, with $\mathrm{RMS}(r) \approx 0.05$ rad/s and a tight spread (roughly $0.045 - 0.055$ rad/s), indicating limited oscillations and a smooth yaw response across the Monte-Carlo runs.

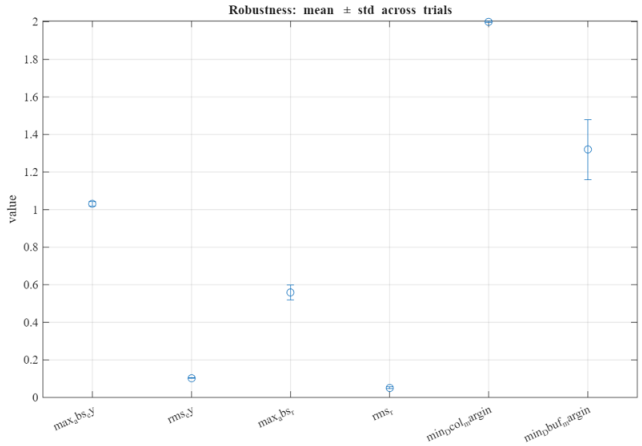

Figure 13: Robustness summary over Monte-Carlo trials (mean ± standard deviation, $N = 20$).

Fig. 13 reports that the maximum absolute lateral tracking error remains close to 1.03 m on average ($\max|e_y| \approx 1.03$ m) with very small variability, indicating that the worst-case lateral deviation is largely insensitive to the imposed uncertainties. The RMS lateral error is approximately 0.10 m ($\mathrm{RMS}(e_y) \approx 0.10$ m) with negligible dispersion, confirming consistently accurate tracking in typical conditions.

In terms of yaw dynamics, the mean peak yaw rate is about 0.55 rad/s ($\max|r| \approx 0.55$ rad/s) with a modest standard deviation ($\approx 0.03 - 0.04$ rad/s), while the yaw-rate RMS stays around 0.05 rad/s ($\mathrm{RMS}(r) \approx 0.05$ rad/s) with a very small spread, which indicates a smooth yaw response and limited oscillations across trials.

Regarding safety, the minimum hard collision margin is tightly concentrated near 2.0 m ($\min D_{\mathrm{col}} \approx 2.0$ m with essentially zero dispersion), confirming that the hard collision-avoidance requirement remains satisfied in all realizations. The minimum conservative buffer margin is lower, with mean a $\min D_{\mathrm{buf}} \approx 1.32$ m and a visible dispersion (std ≈ 0.16 m,

corresponding roughly to a 1σ range of about $1.16 - 1.48$ m). This behavior is expected because D_{buf} includes the additional clearance offset d_0 and is evaluated only during conflict-active intervals; hence, variations in the relative motion during merge/cut-in phases primarily affect D_{buf}, while the hard collision margin D_{col} remains strongly positive.

5 Conclusion

This paper presented a stability-aware fuzzy control framework for autonomous vehicles performing high-speed lane-change maneuvers in mixed traffic. The proposed approach combines a nonlinear single-track vehicle model with an enhanced semi-empirical Pacejka tire formulation to capture the coupled longitudinal–lateral–yaw dynamics under realistic tire-condition effects. Two coordinated Mamdani type-1 fuzzy controllers were developed for steering and longitudinal acceleration, and all membership-function parameters and rule weights were jointly tuned via constrained simulation-based optimization using the Slime Mould Algorithm (SMA). Explicit actuator bounds and a hard collision-avoidance constraint were enforced over the maneuver horizon, while a Lyapunov-inspired penalty was embedded in the objective to suppress oscillations and promote well-damped transient responses.

Simulation results demonstrated rapid convergence of tracking errors ($\approx 2 - 3$ s), smooth steering and acceleration commands, and collision-free lane-change trajectories in the considered scenarios. Relative to an unoptimized fuzzy baseline, the optimized design significantly improved both tracking and stability, reducing peak lateral deviation and yaw-rate oscillations. Monte-Carlo robustness trials under parametric uncertainty, sensor noise, and actuator delays further indicated repeatable closed-loop behavior and maintained positive hard safety margins, while the conservative buffer metric quantified how much additional clearance could be temporarily consumed during conflict intervals.

Future work will focus on hardware-in-the-loop and experimental vehicle validation, systematic robustness evaluation over wider friction/tire-condition ranges, and integration with higher-level planning modules to generate globally efficient references while preserving local stability and safety during aggressive lane changes.

References

[1] M. Ardelt, C. Coester, N. Kaempchen, *Highly automated driving on freeways in real traffic using a probabilistic framework*, IEEE Transactions on Intelligent Transportation Systems, **13**(4) (2012), 1576-1585. https://doi.org/10.1109/TITS.2012.2196273

[2] Q. H. Do, H. Tehrani, S. Mita, M. Egawa, *Human drivers based active-passive model for automated lane change*, IEEE Intelligent Transportation Systems Magazine, **9**(1) (2017), 42-56. https://doi.org/10.1109/MITS.2016.2613913

[3] M. H. Haider, H. Ali, A. Aman Khan, H. Zheng, *Autonomous mobile robot navigation using adaptive neuro fuzzy inference system*, 2022 International Conference on Innovations and Development of Information Technologies and Robotics (IDITR), (2022), 93-99. https://doi.org/10.1109/IDITR54676.2022.9796495

[4] A. Hentout, A. Maoudj, A. Kouider, *Shortest path planning and efficient fuzzy logic control of mobile robots in indoor static and dynamic environments*, Romanian Journal of Information Science and Technology, **27**(1) (2024), 21-36. https://doi.org/10.59277/ROMJIST.2024.1.02

[5] P. Hidas, *Modelling lane changing and merging in microscopic traffic simulation*, Transportation Research Part C: Emerging Technologies, **10**(5-6) (2002), 351-371. https://doi.org/10.1016/S0968-090X(02)00026-8

[6] F. Kamil, et al., *Fuzzy logic-based control for intelligent vehicles: A survey*, In AIP Conference Proceedings, AIP Publishing LLC, (2024). https://doi.org/10.1063/5.0199602

[7] S. Li, et al., *Slime mould algorithm: A new method for stochastic optimization*, Future Generation Computer Systems, **111** (2020), 300-323. https://doi.org/10.1016/j.future.2020.03.055

[8] K. Liu, J. Gong, A. Kurt, H. Chen, *Dynamic modeling and control of high-speed automated vehicles for lane change maneuver*, IEEE Transactions on Intelligent Vehicles, **3**(3) (2018), 329-339. https://doi.org/10.1109/TIV.2018.2843177

[9] Y. Luo, Y. Xiang, K. Cao, K. Li, *A dynamic automated lane change maneuver based on vehicle-to-vehicle communication*, Transportation Research Part C: Emerging Technologies, **62** (2016), 87-102. https://doi.org/10.1016/j.trc.2015.11.011

[10] J. E. Naranjo, C. González, R. Garc, T. D. Pedro, *Lane-change fuzzy control in autonomous vehicles for the overtaking maneuver*, IEEE Transactions on Intelligent Transportation Systems, **9**(3) (2008), 438-450. https://doi.org/10.1109/TITS.2008.922880

[11] J. Nilsson, et al., *If, when, and how to perform lane change maneuvers on highways*, IEEE Intelligent Transportation Systems Magazine, **8**(4) (2016), 68-78. https://doi.org/10.1109/MITS.2016.2565718

[12] Ü. Özgüner, T. Acarman, K. A. Redmill, *Autonomous ground vehicles*, Artech House, 2011.

[13] R. E. Precup, et al., *Problem setting for trajectory planning and cruise control of a connected autonomous electric bus in intersection scenarios with human-driven vehicles to optimize energy, comfort and tracking*, Romanian Journal of Information Science and Technology, **28** (2025), 299-312. https://doi.org/10.59277/ROMJIST.2025.3.05

[14] O. Rodríguez-Abreo, et al., *Fuzzy logic controller for UAV with gains optimized via genetic algorithm*, Heliyon, **10**(4) (2024). https://doi.org/10.1016/j.heliyon.2024.e26363

[15] S. Samonto, et al., *Best fit membership function for designing fuzzy logic controller aided intelligent overcurrent fault protection scheme*, International Transactions on Electrical Energy Systems, **31**(5) (2021), e12875. https://doi.org/10.1002/2050-7038.12875

[16] O. Sharma, N. C. Sahoo, N. B. Puhan, *Recent advances in motion and behavior planning techniques for software architecture of autonomous vehicles: A state-of-the-art survey*, Engineering Applications of Artificial Intelligence, **101** (2021), 104211. https://doi.org/10.1016/j.engappai.2021.104211

[17] K. B. Singh, S. Sivaramakrishnan, *Extended pacejka tire model for enhanced vehicle stability control*, arXiv preprint, (2023), arXiv:2305.18422. https://doi.org/10.48550/arXiv.2305.18422

[18] J. Wen, F. Wang, *Stable levitation of single-point levitation systems for maglev trains by improved cascade control*, Romanian Journal of Information Science and Technology, **27**(3-4) (2024), 348-361. https://doi.org/10.59277/ROMJIST.2024.3-4.08

[19] H. Xue, et al., *Fuzzy controller for autonomous vehicle based on rough sets*, IEEE Access, **7** (2019), 147350-147361. https://doi.org/10.1109/ACCESS.2019.2946663

[20] D. Yang, et al., *Modeling and analysis of the lane-changing execution in longitudinal direction*, IEEE Transactions on Intelligent Transportation Systems, **17**(10) (2016), 2984-2992. https://doi.org/10.1109/TITS.2016.2542109

[21] H. Yu, et al., *Automated vehicle-involved traffic flow studies: A survey of assumptions, models, speculations, and perspectives*, Transportation Research Part C: Emerging Technologies, **127** (2021), 103101. https://doi.org/10.1016/j.trc.2021.103101

[22] L. A. Zadeh, *Fuzzy sets*, Information and Control, **8**(3) (1965), 338-353. https://doi.org/10.1016/S0019-9958(65)90241-X

[23] J. Zhou, et al., *Multiobjective optimization of lane-changing strategy for intelligent vehicles in complex driving environments*, IEEE Transactions on Vehicular Technology, **69**(2) (2020), 1291-1308. https://doi.org/10.1109/TVT.2019.2956504